



# Implementation of a dry deposition module (DEPAC v3.11) in a large eddy simulation code (DALES v4.4)

Leon Geers<sup>1,\*</sup>, Ruud Janssen<sup>1,\*</sup>, Gudrun Thorkelsdottir<sup>1,2,3</sup>, Jordi Vilà-Guerau de Arellano<sup>2</sup>, and Martijn Schaap<sup>1</sup>

<sup>1</sup>TNO, Department of Air quality and Emissions Research, Utrecht, the Netherlands

<sup>2</sup>Meteorology and Air Quality Section, Wageningen University, The Netherlands

<sup>3</sup>Now at: RIVM National Institute for Public Health and the Environment, Center for Environmental Quality, Bilthoven, The Netherlands

\*These authors contributed equally to this work.

**Correspondence:** Ruud Janssen (ruud.janssen@tno.nl)

**Abstract.** High-resolution data on reactive nitrogen deposition are needed to inform cost-effective policies. Large eddy simulation models coupled to a dry deposition module present a valuable tool for obtaining these high-resolution data. In this paper we describe the implementation of a dry deposition module (DEPAC v3.11) into a large eddy simulation code (DALES v4.4), and its first application in a real-world case study. With this coupled model, we are able to represent the turbulent surface-atmosphere exchange of passive and reactive tracers at the hectometer resolution. A land surface module was implemented to solve the surface energy budget and provide detailed information for the calculation of deposition fluxes per land use (LU) class. Both the land surface model and the dry deposition module are extensively described, as well as the inputs that are needed to run them.

To show the advantages of this new modeling approach, we present a case study for the city of Eindhoven in the Netherlands, focusing on the emission, dispersion and deposition of  $\text{NO}_x$  and  $\text{NH}_3$ . We find that DALES is able to reproduce the main features of the boundary layer development and the diurnal cycle of local meteorology well, with the exception of the evening transition. DALES calculates the dispersion and deposition of  $\text{NO}_x$  and  $\text{NH}_3$  in great spatial detail, clearly showing the influence of local LU patterns on small-scale transport, removal efficiencies and mixing characteristics.

## 1 Introduction

Eutrophication and acidification due to atmospheric deposition of reactive nitrogen have widespread impacts on biodiversity (Bobbink et al., 2010; Dise et al., 2011). Across Europe critical nitrogen loads are widely exceeded in protected nature areas, most notably in or close to source regions of ammonia and nitrogen oxides (Jonson et al., 2022). The Netherlands is a densely populated country and has a very productive agricultural sector, a combination leading to the largest emission density of reactive nitrogen compounds in Europe (EMEP/CEIP, 2023). Often, activities emitting large quantities of reactive nitrogen are located in close proximity to nature areas. For example, many farms are located within a kilometer of a nature reserve. In addition,



major roads and highways may cut through or circumvent nature reserves and some of the country's largest industrial facilities border areas declared a nature preservation area. These activities all contribute to total deposition loads on nature areas.

Deposition loads can be seen as a sum of a background deposition caused by a large number of small contributions from distant sources and a local deposition due to nearby sources. Traditionally, these spatial scales have been addressed by different modeling techniques applying chemistry transport models (CTMs) at the regional scale and dispersion models at the local-scale. As the CTMs simulate explicit chemistry on an hour-by-hour basis on a regular grid, they assume instantaneous mixing within their grid cells and thus cannot be used to address near source dispersion and chemistry. In contrast, local scale modeling is often performed with Gaussian plume models driven by statistical meteorological data. These models describe hourly averaged plumes based on wind characteristics, atmospheric stability and downwind surface roughness. Losses due to deposition and chemistry can only be taken into account through very simplified calculation rules and source depletion terms. A number of models combine a plume approach with a trajectory system with a slightly more elaborate accounting of chemical conversion, e.g. OPS (Sauter et al., 2020) and FRAME (Aleksankina et al., 2018; Singles et al., 1998). Both types of models thus have their limitations in representing processes relevant to deposition at the local scale.

Aforementioned local modeling practices prevail due to modest calculation requirements in many (regulatory) applications such as permitting practices. However, a number of applications call for the development of more detailed modeling systems for the local scale. Firstly, for reactive species the processes of turbulent dispersion, chemistry, and deposition take place on similar time and spatial scales and together determine the deposition patterns in a complex landscape. Atmospheric chemistry is often parameterized in these models, which leads to systematic biases in conditions that deviate from the photo-stationary state, especially for fast reacting species such as  $\text{NO}_2$  (Vilà-Guerau de Arellano et al., 1990; Grylls et al., 2019; Zhong et al., 2017). Besides the photo-stationary equilibrium, the  $\text{NO}_2$  atmospheric lifetime of 2 to 12 hours may cause a substantial fraction of the locally emitted  $\text{NO}_x$  to be converted into nitric acid which deposits efficiently. Moreover, the turbulent mixing time scales have been shown to impact the formation of ammonium nitrate (Aan de Brugh et al., 2013; Barbaro et al., 2015), which is supported by reports of ammonium nitrate evaporation impacting ammonia flux measurements (Zhang et al., 1995). Hence, to study the deposition of nitrogen compounds in a complex landscape in detail, a model is required that resolves the turbulent structure of the boundary layer, the chemical interactions and the deposition processes. Secondly, modern observation systems reach temporal and spatial resolutions such that detailed modeling is required to optimize the monitoring design and interpret their results. For example, new satellite missions target resolutions of several hundreds of meters, scales at which plumes will be partially resolved (ESA, 2023). Recent flight campaigns already show the meandering plumes from all kinds of large point sources. Fast response instruments are being used to perform mobile measurements traversing through plumes (Twigg et al., 2022). All these observations do not fit a Gaussian plume representation as they observe an instantaneous realization of the plume at hand. To invert emission strengths from these observation systems, more detailed understanding is needed of the plume behavior and of loss terms between source and receptor. Thirdly, the societal debate on reactive nitrogen deposition and the potential mitigation strategies, as well as the underlying science, calls for the evaluation of the highly parameterized dispersion models that are currently used in many regulatory applications.



55 Models that resolve the turbulent flow and chemical reactions simultaneously are crucial at spatial scales of 100 m and below. Large Eddy Simulation (LES) models in principle have that capacity, since they resolve the atmospheric transport by the largest scales of atmospheric turbulence. They have been developed since the 1970s (Deardorff, 1970) and have been applied mostly to academic cases. In LES modeling, the turbulent flow field defined by the full Navier-Stokes equations is resolved down to certain minimum length and time scales. Below these scales, a sub-grid scale model (SGS) dictates the behavior of the small scale turbulent eddies and the dissipation of turbulent kinetic energy. In that sense, LES offers many benefits above widely applied Reynolds-averaged Navier-Stokes calculations, which only provide time-averaged properties of fluid flow (Blocken, 2015). Recent developments in computational power and coupling to large scale models (Jansson et al., 2019; Van Stratum et al., 2019; Schalkwijk et al., 2015) have enabled the application of LES on larger spatial and temporal scales than before. Several LES codes are currently being developed towards application in air quality though the development of modules that represent, for instance, the flow around buildings (Tomas et al., 2015), gas-phase chemistry (Vilà-Guerau de Arellano et al., 2011; Kim et al., 2012; Khan et al., 2021) or anthropogenic emissions (Khan et al., 2021). These developments have significantly improved the representation of real-world cases (Maronga et al., 2020; Suter et al., 2022).

Dry deposition of gaseous and aerosol species on the (vegetated) land surface has not been explored much using LES models. Barbaro et al. (2015) have studied gas-aerosol partitioning for ammonium nitrate with DALES, the Dutch Atmospheric Large Eddy Simulation model (Heus et al., 2010). They used a simplified resistance model (e.g. Wesely (1989)) including the aerodynamic resistance, a quasi laminar sub-layer resistance (depending on the molecular diffusivity of the gas) and a bulk surface resistance for a land use consisting of grass only. Clifton and Patton (2021) applied the National Center for Atmospheric Research (NCAR) LES model, coupled to a multi-layer model of the vegetation canopy with a simplified chemical mechanism. They focused on the ozone deposition to canopy and soil, and particularly on the influence of turbulence on the deposition. Subsequently, Clifton et al. (2022) extended the model with a chemical model of 41 reactions and 19 gases for ozone,  $\text{NO}_x$  ( $= \text{NO} + \text{NO}_2$ ),  $\text{HO}_x$  ( $= \text{OH} + \text{HO}_2$ ), and isoprene chemistry. Although the dry deposition process description has also recently been included in the PALM LES code (Khan et al., 2021), there has not been specific attention to its application.

Our overall goal is to study the process affecting nitrogen deposition at the landscape scale using the DALES system. In this work, we coupled a dry deposition module to the LES code, with the goal of enabling the representation of dry deposition of trace gases over a realistic land use mosaic. Our approach focuses on the application of the well established dry deposition parameterization DEPAC (Deposition of Acidifying Compounds; Van Zanten et al. (2010)) in DALES. To demonstrate the capability of the model to simulate tracer dispersion and dry deposition, we set up a case study over the city of Eindhoven, the Netherlands, which is the fourth largest city in the Netherlands. In contrast to other large cities in the Netherlands, its inland location ensures that we can use the meteorological forcing as applied here, since there is no coastline or large water bodies in the domain. The city is surrounded by major highways and an airport, and is embedded in an area with intensive animal husbandry. Hence, it is one of the regions where the reactive nitrogen emissions are greatest and result in exceedance of the critical loads in the nature areas adjacent to the city. In our current analysis, we focus on the dispersion and dry deposition of two passive tracers ( $\text{NO}_x$  and  $\text{NH}_3$ ) and their dependence on atmospheric and LU properties. Chemical conversions are not yet included in this study.



90 This paper is organized as follows: in Section 2, we describe the DALES model and the DEPAC dry deposition module, as well as the implementation of DEPAC in DALES. Next, we apply the system in a case study for Eindhoven (Section 3). The results of the case study are shown in Section ???. This case study is a first demonstration of dry deposition at high resolution in a complex landscape. Therefore, we will focus on the qualitative aspects and highlight directions for future development. Finally, in Section 4, we summarize our conclusions.

## 95 2 Model description

### 2.1 DALES

The Dutch Atmospheric Large Eddy Simulation (DALES) is rooted in the LES code of Nieuwstadt and Brost (1986) and Cuijpers and Duynkerke (1993). The model resolves turbulent transport processes based on the filtered Navier-Stokes equations combined with the Boussinesq approximation. DALES uses one-and-a-half-order closure to parameterize subfilter-scale processes. A complete description DALES v3.2 is given by Heus et al. (2010). Since version 3.2, a few additions were made, including improved restart possibilities, new advection schemes, an improved radiation model and optimized subgrid calculations.

DALES has been applied in studies on the transport and chemical conversion of reactive species in the boundary layer. Vinuesa and Vilà-Guerau de Arellano (2003) studied the effect of turbulence on reactive tracer transport, and Vilà-Guerau de Arellano et al. (2005) studied the influence of cumulus clouds on transport of reactive tracers. In a series of case studies over tropical forests, Vilà-Guerau de Arellano et al. (2009) used DALES to study the diurnal cycle of isoprene emissions, Vilà-Guerau de Arellano et al. (2011) performed case studies on the diurnal cycle of concentrations of reactive species, and Ouwersloot et al. (2011) studied the influence of turbulence on the reactivity of chemical species. These studies did not take dry deposition of trace gases into account.

110 In an idealized DALES experiment, Aan de Brugh et al. (2013) studied the gas-particle partitioning of ammonium nitrate in the convective boundary layer at mid-latitudes. They suggest that turbulent mixing in the CBL causes horizontal and temporal variability in aerosol nitrate mixing ratios, which leads to an apparent downward flux of ammonium nitrate which might be interpreted as nitrate deposition. Barbaro et al. (2015) expanded that case study by including surface-exchange of ammonium nitrate and related gas-phase species in a simplified way. Recently, Schulte et al. (2022) studied the turbulent dispersion of NH<sub>3</sub> with DALES, with the goal of assessing the representativity of NH<sub>3</sub> observations. In their simulations, they prescribed a constant deposition flux for NH<sub>3</sub>, based on annual average observations.

### 2.2 Land surface module

The land surface and the atmosphere above it form a tightly coupled system on diurnal (and longer) time scales (Betts, 2004; Van Heerwaarden et al., 2010). The direction and strength of the exchange of heat, moisture, and momentum, is driven by this coupling. Moreover, land use plays an important role in dry deposition, because the properties of the land surface regulate the



uptake of pollutants. Therefore, the relationship between deposition fluxes of reactive compounds, the (vegetated) land surface, and the heat and moisture fluxes is integral to our approach of coupling a deposition module to DALES.

The state of the vegetation, the soil and their exchanges of heat and water with the atmosphere in DALES is described by a Land Surface Model (LSM) that is based on the Tiled ECMWF Scheme for Surface Exchanges over Land with revised hydrology (HTESSEL) land surface scheme (ECMWF, 2021; Balsamo et al., 2009). In HTESSEL, sub-grid surface types are represented by tiles. Each tile represents a LU type for which an energy balance equation is solved. This results in a sensible (H) and latent (LE) heat flux per tile, which is then aggregated to a grid cell. Soil moisture content and soil temperature are calculated in a 4-layer soil model. Precipitation and dew fall is collected in an interception layer. Canopy conductance can be calculated in two different ways in HTESSEL: following the Jarvis Stewart approach or following a plant physiology based approach (A-gs). Here, we followed the former approach. Monin-Obukhov Similarity Theory (MOST) is used to estimate the resistances associated with transport between the lowest model level and the land surface.

We made modifications in the LSM to enable the coupling with the deposition module. Most importantly, we made the number and types of land use classes available flexible. In that way, the land use (LU) types relevant for dry deposition can be selected flexibly, and relevant properties can be assigned. Here, we aligned the LU types with those available in DEPAC (see Table B1).

### 2.3 Description of the DEPAC deposition module

To account for dry deposition in local air quality models, one of two approaches is generally followed. The first and simplest approach is the assumption of a constant deposition velocity that is tabulated for each species. This approach has three important downsides. First, there is a significant influence of the wind speed and the turbulence generated near the surface on the transport of species to the surface which is not covered when assuming constant deposition velocity. It is therefore important to incorporate the surface roughness and the surface type in the calculation of dry deposition of both gaseous and aerosol species. Second, variations in plant physiology, temperature, relative humidity and radiation play an important role in determining the dry deposition velocity (see for instance Emberson et al. (2000b)), whereas a constant deposition velocity only contains static influences. Third, the concept of a constant deposition velocity is also inappropriate since it assumes a constant deposition velocity with height near the surface which is not holding for chemically reactive species like NO<sub>x</sub> (?). Including these parameters in the parametrization of dry deposition is essential to get insight into diurnal and seasonal cycles, the effect of meteorology on deposition, and to get a realistic representation of atmospheric concentrations and deposition.

The second and most widely used approach, is the resistance model attributed to Wesely (1989), who modelled the deposition velocity  $V_d$  as the reciprocal sum of three resistances: the aerodynamic resistance  $R_a$ , the quasi-laminar sub-layer resistance  $R_b$ , and the canopy resistance  $R_c$ .

$$V_d = \frac{1}{R_a + R_b + R_c} \quad (1)$$

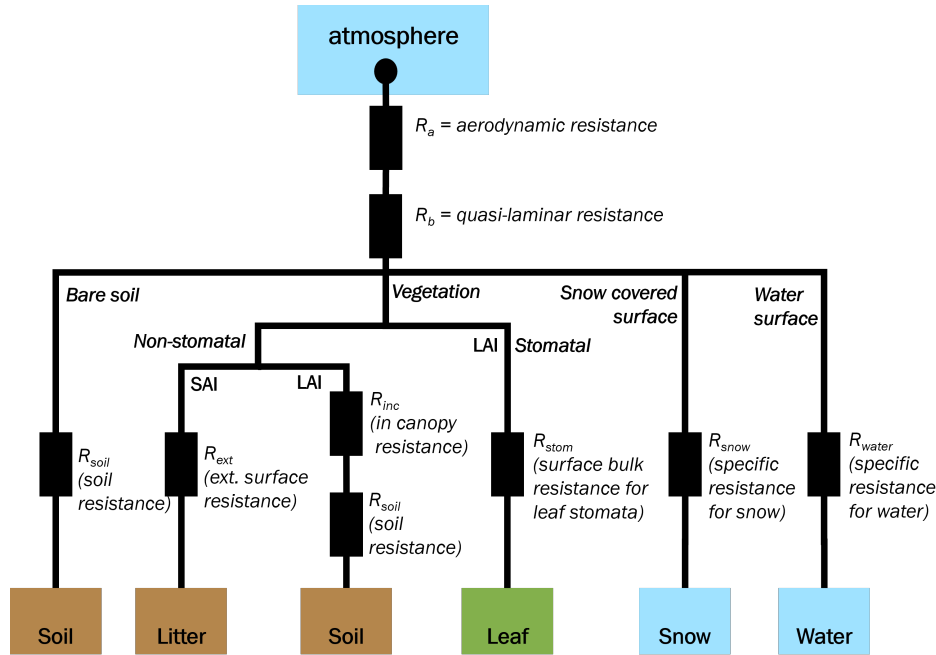


**Figure 1.** Schematic representation of the dry deposition model (DEPAC) in DALES.

In this work, the DEPAC deposition module is used, which is an implementation of the resistance model. A schematic representation of the DEPAC model is shown in Figure 1, with its deposition pathways to vegetated and non-vegetated surfaces, each with their own specific parameters. It offers a fine grained differentiation of deposition on 9 different land use classes.

155 The calculation of the aerodynamic resistance  $R_a$  is based on the meteorological conditions and the surface roughness.  $R_a$  is common to all species and determined from the stability of the atmosphere and the surface roughness. Because the surface roughness depends on the land use type, in DALES we calculate the  $R_a$  per land use type in a grid cell.

$$R_a = \frac{1}{u^* \cdot \Phi_h} \quad (2)$$

where  $u^*$  is the friction velocity and  $\Phi_h$  is a parameter that depends on atmospheric stability and is calculated from MOST  
 160 (Businger et al., 1971).

The quasi-laminar resistance  $R_b$  is determined from the friction velocity and the diffusivity of the species in air. Even though there is a species dependence (in the Schmidt number) in  $R_b$ , it normally plays a minor role, because the quasi-laminar layer is usually very thin and  $R_b$  is therefore small.

$$R_b = \frac{2}{\kappa \cdot u^*} \cdot \left( \frac{Sc}{Pr} \right)^{(2/3)} \quad (3)$$



165 in which  $\kappa$  is the Von Kármán constant,  $Sc$  is the dimensionless Schmidt number, defined as the ratio between the kinematic viscosity of the air and the mass diffusivity of the species in air, and  $Pr$  is the dimensionless Prandtl number, defined as the ratio between the kinematic viscosity of the air and the heat diffusivity of the air (definition according to Wesely and Hicks (1977)).

The canopy resistance  $R_c$  is the resultant of three parallel resistances: the stomatal resistance, the soil resistance and the external surface resistance. The canopy resistance  $R_c$  is calculated from stomatal and non-stomatal conductances and resistances based on the model of Erisman et al. (1994).

$$R_c = \left( \frac{1}{R_{stom}} + \frac{1}{R_{soil,eff}} + \frac{1}{R_w} \right)^{-1} \quad (4)$$

Non-stomatal transport is split into the transport to external surfaces (cuticles and other surfaces, represented by the resistance  $R_w$ ) and transport through the canopy to the soil ( $R_{soil,eff}$ ). For the latter, a distinction is made between snow covered and open soil. The stomatal resistance  $R_{stom}$  is implemented according to Emberson et al. (2001). Stomatal conductance is controlled by the vegetation type, its phenological state, temperature, relative humidity, insolation, and soil water potential.

In general, there are two main variants of this resistance approach. One assumes zero concentration of the species on the deposition surface; the deposition flux  $F_{dep}$  is modelled as the product of the deposition velocity and the concentration in the air above the surface  $\chi_{atm}$  (e.g. Simpson et al., 2012). Though it performs well for compounds that are completely absorbed on the surface, it induces possible overestimation of the deposition fluxes and does not anticipate re-emission of species from the surface into the atmosphere. Especially for  $NH_3$  during growing seasons, this may result in unrealistic deposition fluxes (Wichink Kruit et al., 2007). The ammonium reservoir in the surfaces provides a partial pressure of ammonia above the surface. When ammonia concentrations are above this so-called compensation point deposition occurs, whereas emission takes place when the ambient ammonia concentrations are below the compensation point. Hence, the exchange is bi-directional. The resulting flux is calculated with:

$$F_{dep} = -V_d \cdot (\chi_{atm} - \chi_{comp}) \quad (5)$$

The compensation point is defined for the stomatal and external surface deposition routes, and its parametrization is given in Section 2.3.1.

At this moment, DEPAC uses a dedicated land surface model that is different from HTESSEL. While HTESSEL is used for the calculation of energy and moisture fluxes, the land surface model in DEPAC is dedicated to the deposition flux calculations. Future development plans include the integration of these two modules, but at this moment, they are used in parallel. In dry conditions, this is not a problem, but there is a caveat to this approach regarding wet surfaces. HTESSEL defines a dedicated land surface class for wet surfaces, regardless the underlying land surface. DEPAC's land surface model uses a flag for each land surface type that signals whether it is dry or not. Due to these different implementations, cases with wet soil and/or canopy cannot be simulated properly, as the current implementation of DEPAC ignores the fact that the soil/canopy is wet (it assumes





dry conditions). Here, we circumvented this problem by selecting dry days in a period with little or no rain. In addition, a sensitivity analysis in a related project pointed out that the effect of switching between dry and wet land on the deposition fluxes of  $\text{NH}_3$  is not very strong.

### 2.3.1 Canopy exchange

200 The first term on the right in Equation 4, the deposition resistance for stomatal exchange, is defined in Equation 6 below. Per LU class, a maximum conductivity  $G_s^{max}$  is defined, which signifies the conductivity in the case of fully opened leaf stomata. The stomata may not to be fully open due to a number of causes; for each of these, a parameter between zero and one is multiplied with  $G_s^{max}$  to scale the transport.  $f_{phen}$  is the correction factor for plant phenology,  $f_{swp}$  corrects for the soil water potential,  $f_{vpd}$  for the vapour pressure deficit,  $f_T$  is a temperature correction, and  $f_{PAR}$  is the correction for photo-active  
 205 radiation (Emberson et al., 2000b, a).

$$R_{stom} = (G_s^{max} \cdot f_{phen} \cdot f_{swp} \cdot f_{vpd} \cdot f_T \cdot f_{PAR})^{-1} \quad (6)$$

, where the correction factor for phenology  $f_{phen}$  and the correction factor for soil water potential  $f_{swp}$  are both assumed equal to 1.0, since the influence of phenology is negligible for the land use classes in DEPAC and soil water potential is expected to be of limited influence in our study area. The seasonal dependence is covered by the use of a leaf area index that varies with  
 210 the growing season of the vegetation.

Specifically for  $\text{NH}_3$ , the stomatal compensation point  $\chi_s$  is calculated from an equilibrium correlation (Wichink Kruit et al., 2007).  $\Gamma_s$  is the dimensionless ratio between the apoplastic molar  $\text{NH}_4^+$  and  $\text{H}^+$  concentration given by (Wichink Kruit et al., 2010):

$$\chi_s = \frac{2.75 \cdot 10^{15}}{T_s + 273.15} \exp\left(\frac{-1.04 \cdot 10^4}{T_s + 273.15}\right) \cdot \Gamma_s \quad (7)$$

$$215 \quad \Gamma_s(T_s) = 362 \cdot \chi_{a,4m,long term} \cdot 4.7 \cdot \exp(-0.071T_s) \quad (8)$$

in which  $\chi_{a,4m,long term}$  is the 'long term' mean concentration of  $\text{NH}_3$  at 4m above the ground ( $\mu\text{g m}^{-3}$ ) and  $T_s$  is the leaf surface temperature ( $^{\circ}\text{C}$ ).

External leaf surface exchange is covered by the resistance  $R_w$ , as defined in Eq. 9, with  $RH$  being the relative humidity in %, and  $\alpha = 2\text{s m}^{-1}$  and  $\beta = 12$  are empirical model parameters (Sutton and Fowler, 1993). DEPAC uses an additional  
 220 correction factor dependent on the surface area index (SAI) to account for differences between SAI of the local vegetation type and the SAI at the measuring site where the compensation point  $\chi_w$  was determined (Haarweg, Wageningen, The Netherlands).  $T_w$  is the surface temperature ( $^{\circ}\text{C}$ ) and  $\Gamma_w$  is the dimensionless molar ratio between the  $\text{NH}_4^+$  and  $\text{H}^+$  concentrations in the external leaf surface water (Van Zanten et al., 2010; Wichink Kruit et al., 2010).

$$R_w = \frac{SAI_{Haarweg}}{SAI} \cdot \alpha \exp\left(\frac{100 - RH}{\beta}\right) \quad (9)$$





225 For freezing conditions, a fixed value of  $R_w$  is assumed.

A compensation point can be calculated for the external surfaces with the same relation as for the stomatal compensation point, only  $\Gamma_w$  is substituted for  $\Gamma_s$ . Specifically for  $\text{NH}_3$  over grassland,  $\Gamma_w$  is defined according to the empirical relation in Equation 10, in which  $\chi_{a,4m}$  is the compensation point at 4 m (Wichink Kruit et al., 2010).

$$\Gamma_w = 1.84 \cdot 10^3 \cdot \chi_{a,4m} \cdot \exp(-0.11T_s) - 850 \quad (10)$$

### 230 2.3.2 Soil exchange

Depositing species first have to travel through the canopy before they reach the soil. The effective soil resistance is therefore calculated as the sum of the in-canopy resistance  $R_{inc}$  and the soil resistance  $R_{soil}$ :

$$R_{soil,eff} = R_{inc} + R_{soil} \quad (11)$$

235 The in-canopy resistance is a function of LU type, the height of the vegetation  $h$ , the SAI and the friction velocity  $u^*$  (Van Pul et al., 2008):

$$R_{inc} = \begin{cases} \frac{b \cdot h \cdot SAI}{u^*} & u^* > 0, \text{ arable land, permanent crops, forest} \\ 1000 \text{ s m}^{-1} & u^* \leq 0, \text{ arable land, permanent crops, forest} \\ 0 \text{ s m}^{-1} & \text{water, urban, desert} \\ \infty \text{ s m}^{-1} & \text{grass, other} \end{cases} \quad (12)$$

The SAI depends on the leaf area index (LAI) and the LU type. Some LU classes have no SAI ( $SAI = 0$  for water, barren land, urban), some have a constant value ( $SAI = b_{SAI}$  for arable land, grassland and semi-natural land) and others depend on the LAI ( $SAI = a_{SAI} \cdot LAI (+b_{SAI})$  for permanent crops and forests).

240 The parameters of the in-canopy resistance are defined for 9 different LU classes (see Table A1). The LAI is a function of the time of year and the growing season per LU class (see Van Zanten et al., 2010).

The soil resistance is species dependent and, to a lesser extent, LU dependent (except for frozen, wet, and snow covered soil). For  $\text{NH}_3$ ,  $\text{NO}_2$ , and  $\text{NO}$ , the values are presented in Table A2. These values are based on Erisman et al. (1994), but adapted to the values used in the DEPAC v3.11 implementation in LOTOS-EUROS v2.2 (Manders et al., 2022). Finally, the  
 245 compensation point of the soil can be calculated similar to the stomata (Equation 7) with  $\Gamma_{soil}$  substituted for  $\Gamma_s$ , the value of which is also given in Table A1.

### 2.4 Initial and boundary conditions

The bottom boundary condition for DALES is formed by the soil and LU properties. Representation of LU properties is especially important for dry deposition calculations. We use the TOP10NL LU map at 10 x 10 m<sup>2</sup> (PDOK, 2023) that is



translated to the land surface types defined in DEPAC according to Table B1. Soil type follows the BOFEK soil map Heinen et al. (2022) and soil hydraulic properties (Van Genuchten, 1980).

For meteorological variables, we apply doubly-periodic boundary conditions, which means that forcings are horizontally homogeneous but vary in time and height (Van Stratum et al., 2023). In this approach, the initial conditions (atmosphere and soil) and a number of time and height varying large-scale processes acting as forcings on the LES domain, are derived from routine meteorological variables. These processes, partly in the form of a tendency of a state variable like temperature, humidity, or wind, are then added to the prognostic LES equations. The energy balance calculation is very sensitive to soil moisture and therefore needs to be initialized at realistic value. The open-source Python package "Large-eddy simulation and Single-column model - Large-Scale Dynamics" or (LS)<sup>2</sup>D (Van Stratum et al., 2023) was used to create initial and boundary layer profiles as input for DALES (sources available from <https://github.com/LS2D/LS2D>) from ERA5 reanalysis data (Hersbach et al., 2020).

## 2.5 Anthropogenic emissions

For realistic simulation of passive and reactive tracers at resolutions of tens of meters, detailed information is needed about their emissions at this scale. The emissions of NO<sub>x</sub> and NH<sub>3</sub> we use are based on the official gridded emissions for the Netherlands (the Dutch Emission Registration, ER) for 2018 (RIVM, 2018). The official data contains emissions from more than 700 source types, which are aggregated into 15 sectors. Each source type gets assigned a spatial fraction map that is used to downscale the emissions. A fraction map describes the fraction of the emissions in each 1 x 1 km<sup>2</sup> grid cell that is assigned to the 50 x 50 m<sup>2</sup> grid cells. A total of 12 fraction maps were developed. Hourly emission fluxes are calculated from annual emission totals using fixed monthly, daily and hourly time profiles. This spatial and temporal interpolation, however, creates a large uncertainty in the emission dataset, which will cause uncertainty in the timing and magnitude of emission peaks on a given day and therefore in the calculation of concentrations.

For the industry, households, and commercial activities the Basisregistratie Adressen en Gebouwen (BAG) is used (Kadaster, 2024). The BAG contains information on locations of buildings, number of addresses in each building, their size, and their function, which we use to link each building to one of these three categories. The number of addresses is used to calculate the fractions. A national database of the road network (Nationaal Wegenbestand, 2021 (NWB, 2024) was used to make fraction maps for road transport on different road types (highways, main roads, and residential roads), based on the total road length within each grid cell. For agricultural activities, fractions maps were made for livestock, arable land, and general agricultural activities, based on the Basisregistratie Gewaspercelen (BRP) dataset with information on locations of agricultural plots and crop types (NGR, 2024). For rail roads a map of rail road tracks is used (Prorail, 2020) and for inland shipping we use inland waterways from the same database as the road network (NWB, 2024). Finally, we use a population density map at 100 m resolution for several other source types (CBS, 2023).

For the major point sources (mainly industrial), exact locations and emission height are provided. For non-point sources the emission height is at ground level. Plume rise has not yet been implemented in DALES. The effect of this is limited in this study since there are only a few stacks in the current domain. In the current approach, emissions on city roads appear much less intense than on highways (by a factor of 50, approximately). This is caused by the way emissions are estimated

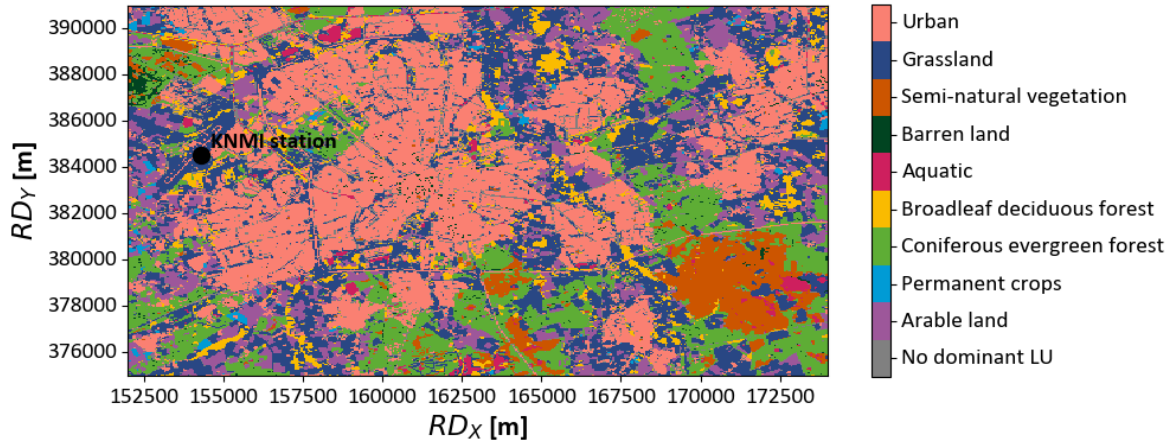


**Figure 2.** Map of the Eindhoven domain showing the land use and the locations of the KNMI measurement station (black dot). Map is plotted using Rijksdriehoeks (RD) coordinates (EPSG 28992).

and downscaled in our current emissions preprocessor. It is still under development; work is being done on the development  
 285 of a more dynamic emission model, which does not imply fixed time profiles, but takes seasonal, meteorological, and environmental factors into consideration. For example, the spatio-temporal variability of ammonia emissions is strongly dependent on agricultural practices, livestock distribution, crop distribution and meteorology (Ge et al., 2023).

### 3 Eindhoven case study

To demonstrate the ability of DALES coupled to a dry deposition scheme to represent nitrogen transport and deposition at high  
 290 spatial resolution, we performed simulations for a full diurnal cycle over a domain around the city of Eindhoven (Figure 2). We chose a day with clear-sky convective conditions (16 June 2022). The month of June in 2022 was warm with a lot of sunshine, but also a lot of rainfall in the Netherlands. The day of our case study fell in a sunny and dry weather period that started the 9<sup>th</sup> of June. The wind direction during this period was mostly from the East, bringing warm and dry air masses. On the day after our case study (June 17<sup>th</sup>), temperatures increased to tropical values (above 30°C). The size of the model domain is 22 x  
 295 16 km<sup>2</sup>, and it is divided into 440 x 320 grid cells of 50 x 50 m<sup>2</sup> each. In the vertical direction, the domain extends up to 8.5 km and it is divided into 128 levels. Near the surface, the level thickness  $\Delta z$  is 20 m, and it gradually increases to 95 m at the top of the domain according to the equation  $\Delta z = \Delta z_0 \cdot (1 + 0.009)^{iz}$ , where  $\Delta z_0$  is the depth of the bottom layer and  $iz$  is the index of the vertical grid.

Hourly observations of standard meteorological variables were available from the KNMI weather station at Eindhoven air-  
 300 port (KNMI, 2024b), station no. 370). Attenuated backscatter profiles from the CHM15k ceilometer at Maastricht Aachen airport were retrieved from KNMI (KNMI, 2024a). They provide daily aggregated files at five sites in the Netherlands, Maastricht Aachen airport being the closest to Eindhoven.



The profiles of  $\text{NO}_x$  and  $\text{NH}_3$  concentrations were initialized to typical values in a shallow boundary layer, since the calculations start at night.  $\text{NO}_x$  was set to 1.0 ppb, from the surface up to 200 m, and 0.5 ppb up to 1250 m high, to simulate the residual layer of the previous day. For  $\text{NH}_3$ , there is only the 200 m boundary layer with a concentration of 2.7 ppb. The concentration values are typical background concentrations measured in and around Eindhoven. Finally, it is important to note that the present calculations do not include atmospheric chemistry yet, so only emission, transport, and deposition are calculated.

### 3.1 Diurnal cycle, vertical mixing

Calculated sensible heat flux (H) and latent heat flux (LE) data from the DALES simulation were compared to the original ERA5 data that was used as forcing (see Figure 3). The sensible heat flux becomes positive around 7:00 local time and peaks around 14:00 LT. Overall, the simulations match ERA5 data well, except for the hours around midday, when the sensible heat flux is larger by about  $100 \text{ W m}^{-2}$  in DALES, and the latent heat flux is smaller by about  $50 \text{ W m}^{-2}$ . A possible explanation is the difference in local LU properties in DALES compared to the ERA5 dataset. DALES in the current setup includes 9 LU types (Section 2.4), whereas the ECMWF IFS only includes 5. Moreover, the resolution of the TOP10NL map in DALES is much higher than the LU map from ECMWF IFS (10 m versus 1 km), so the local landscape is represented in more detail. This leads to differences in the radiative properties of the surface, which will affect the amount of soil moisture and the surface energy balance.

The virtual potential temperature, specific humidity, and wind speed and direction are presented in Figure 4, together with reanalysis data from the ERA5 dataset. ERA5 data are available on a  $0.25^\circ \times 0.25^\circ$  resolution, corresponding to a  $17 \times 28 \text{ km}^2$  area around Eindhoven, compared to the present domain averaged DALES results on an area of  $22 \times 16 \text{ km}^2$ . Downscaling of the meteo quantities from ERA5 is handled well by DALES, since all quantities follow the ERA5 data closely, though the wind speed is slightly underestimated.

Local observations from a weather station at Eindhoven Airport are also plotted in the figure. Since the wind speed is quantized down to integer values and the wind direction down to  $^\circ$ , the standard deviations of the measurement errors are approximately  $0.29 \text{ m s}^{-1}$  and  $3^\circ$ , respectively. There is a slight difference with the observations. The virtual potential temperature shows a 1-2 degree deviation, with a positive model bias during daytime and a negative bias after sunset. This is likely caused by the difference between the lowest model level (from 0 to 20 m above ground level) and the measurement height (2 m). The specific humidity matches within  $0.002 \text{ kg kg}^{-1}$ , but there is a 2-3 hr shift of a trough in the morning. Wind speed shows stronger deviations: up to  $2 \text{ m s}^{-1}$  speed differences.

Vertical profiles of virtual potential temperature ( $\theta_v$ ) show the development of a well-mixed convective boundary layer in the morning and the formation of a stably stratified nocturnal boundary layer at night (Figure 5a). The wind speed in the mixed layer ranges from  $4 \text{ m s}^{-1}$  during the daytime to  $7 \text{ m s}^{-1}$  in the early morning of June 17<sup>th</sup> (Figure 5c). The  $\theta_v$ -profile indicates a boundary layer evolution from 250 m at 06:00 LT to about 1250 m at 12:00 LT and below 200 m during the night (00:00 LT).

Comparison with ceilometer data at Maastricht Aachen airport is shown in Figure 5d. The colors depict the attenuated back-scatter signal of the ceilometer and the black line is the boundary layer height calculated by DALES. Although the

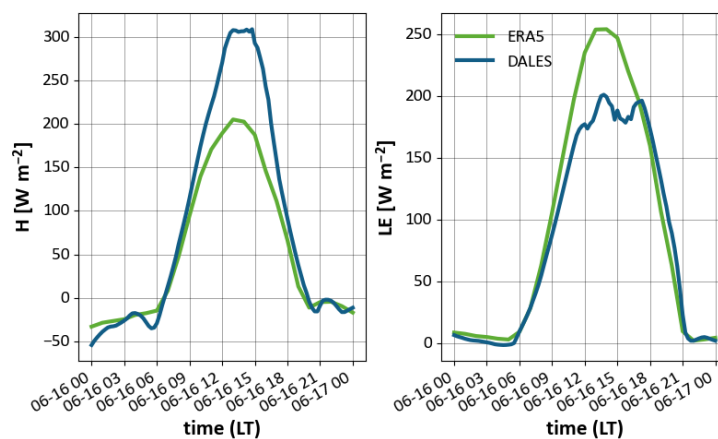


**Figure 3.** Sensible and latent heat fluxes averaged over domain from ERA5 (green) and DALES (blue).

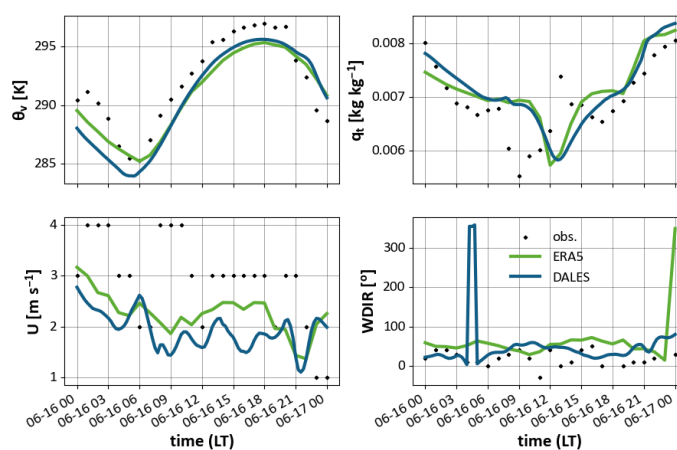


**Figure 4.** Time series of virtual potential temperature, specific humidity, wind speed and wind direction from DALES (blue), ERA5 (green) and observations (dots) on 16 June 2022.



measurement station is approximately 100 km from Eindhoven, the trend should be comparable. The development of the boundary layer calculated from DALES fits the ceilometer data well up to about 21:00 LT, after which the modeled boundary layer height shows a sharp decrease, whereas the ceilometer data show a more gradual decrease, taking about 1.5 hours to decrease to its nocturnal value. This is likely related to the evening transition, during which the strength of the convective turbulence decreases, as buoyancy disappears as its driving force, and a shallow nocturnal boundary layer is formed (Darbieu et al., 2015). During this transition, turbulent length scales decrease to sizes that cannot be resolved at the 50 m resolution of our simulations. The much smaller eddies that dominate the evening atmosphere will be of comparable or even smaller scale than the cell size, which means that most of the turbulence is covered by the sub-grid scale model. Simulations at 25 m resolution (which is the lower bound currently set by the emission downscaling) did not lead to improvements in the representation of the evening transition. A horizontal resolution of  $\approx 10$  m would be more appropriate to simulate the transition to a stable boundary layer (Beare et al., 2006). At night, boundary layer heights of 0 m are diagnosed due to the use of the maximum  $\Delta\theta_v/\Delta h$  as criterion. This approach is valid under convective conditions only, when the boundary layer is capped by a clear temperature inversion. Figure C1 shows boundary layer heights from the same simulation diagnosed with different approaches.

In conclusion, the evaluation of the meteorological variables shows that the DALES configuration applied in this study is able to downscale the ERA-5 meteorological situation successfully. As expected, the different LU classification induces slight differences in the latent and sensible heat fluxes. The only caveat is that the collapse of the boundary layer is quite sudden, which will negatively impact the modelled pollutant concentrations as the mixing after the evening rush hour is clearly underestimated.

### 3.2 NO<sub>x</sub> and NH<sub>3</sub> emissions, dispersion and deposition

Maps of the downscaled NO<sub>x</sub> and NH<sub>3</sub> emissions at a resolution of 50 x 50 m<sup>2</sup> and their time profiles are shown in Figure 6. NO<sub>x</sub> emissions are assumed to consist of 97% NO and 3% NO<sub>2</sub>. The maps show the emissions of 06:00 LT, before the morning rush hour. The NO<sub>x</sub> emissions range over 3 orders of magnitude with very low values in the rural areas, increasing in the urban areas moving closer to the city center, to their maximum values on the highways. The time profile shows two clear peaks during the morning and evening rush hours, when the emissions from traffic dominate, intermediate values during the day, and low values at night. As traffic is a relevant source of ammonia in large urban areas (Wen et al., 2023), we can identify the highways as strong emitters of NH<sub>3</sub>, in a way similar to NO<sub>x</sub>. Some strong agricultural NH<sub>3</sub> sources can also be found in the rural areas on the western, northeastern, and southeastern edges of the domain. The NH<sub>3</sub> emissions show a similar temporal profile as the NO<sub>x</sub> emissions, but with values that are about an order of magnitude lower. The time profiles mainly reflect the diurnal cycle in traffic emissions, with rush hour peaks in morning and end of afternoon. Diurnal cycles for sectors like industry and agriculture have a more flat profile over the day.

The resulting vertical profile of the mean NO<sub>x</sub> concentration over the domain shows a trend similar to the boundary layer development (Figure 7a). This demonstrates the mixing of the emitted NO<sub>x</sub> over the whole boundary layer. The concentration peaks near the surface in the morning and evening, caused by the rush hour emissions and the low boundary layer into which these emissions are mixed. Near the top of the convective boundary, NO<sub>x</sub> mixing ratios are diluted due to entrainment of NO<sub>x</sub>

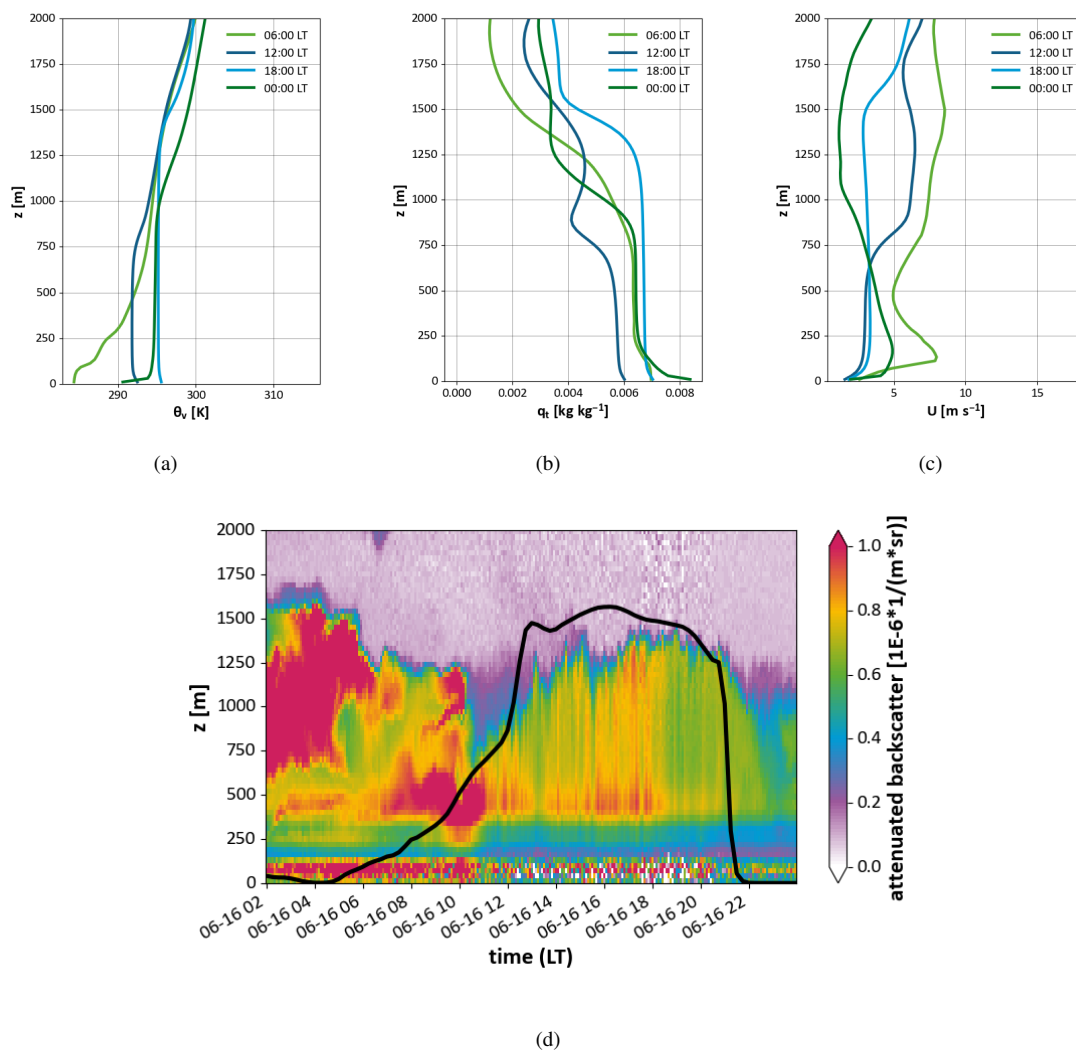


**Figure 5.** Vertical profiles of virtual potential temperature  $\theta_v$  (a), total specific humidity  $q_t$  (b) wind speed  $U$  (c) and boundary layer height and ceilometer backscatter profile on 16 June 2022 (d)



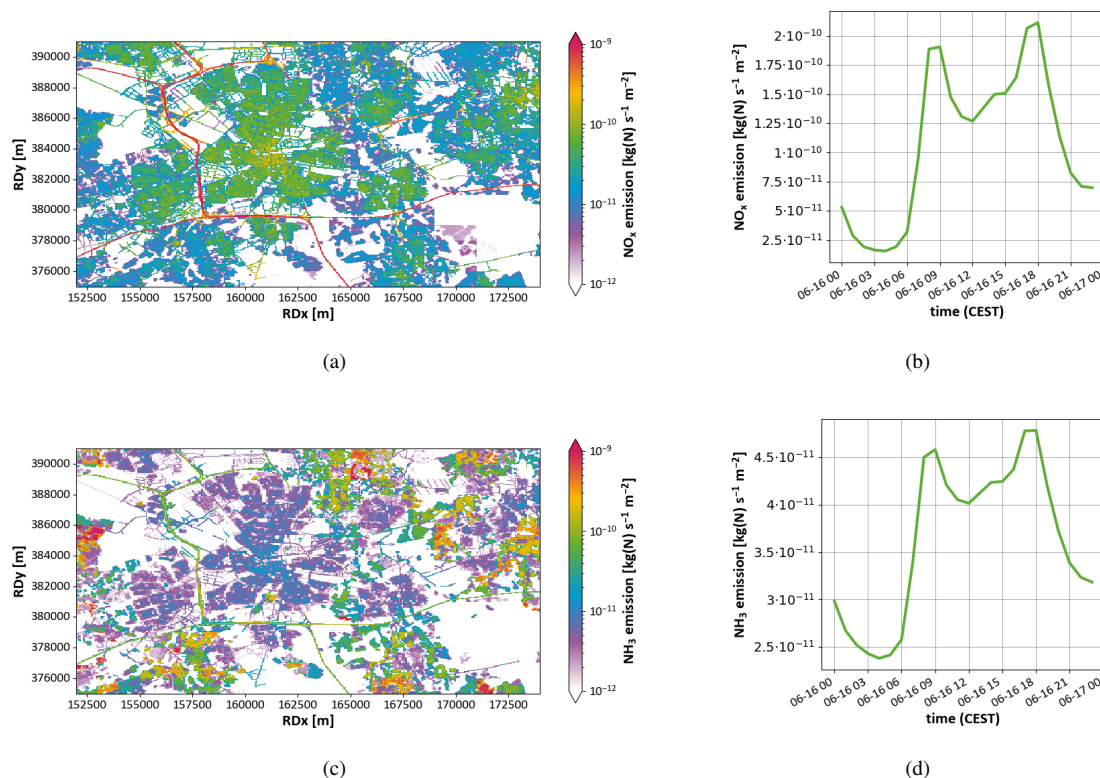


**Figure 6.** Spatial distribution of  $\text{NO}_x$  (a) and  $\text{NH}_3$  (c) emissions (at 06:00 LT) and the emissions time profiles of  $\text{NO}_x$ (b) and  $\text{NH}_3$  (d). Maps are plotted using Rijkdsdriehoeks (RD) coordinates (EPSG 28992).

poor air from the free troposphere. The  $\text{NO}_x$  turbulent flux profile shows a positive flux throughout the boundary layer at all times during the simulation. This means that emission and upward mixing dominate over dry deposition and entrainment. This is expected for a tracer with strong sources over the whole domain. In addition, the dry deposition flux of  $\text{NO}_x$  is significantly lower than the dry deposition flux of  $\text{NH}_3$ . The highest fluxes are found at 12:00 and 18:00 LT when both emissions and vertical mixing are strong (Figure 7b).

For  $\text{NH}_3$ , we find a negative concentration gradient from the surface to the boundary layer background concentration of 2.7 ppb at 12:00, 18:00 and 00:00 LT, but a positive gradient at 06:00 LT (Figure 7c). This positive gradient is caused by dry deposition. In the early morning, the uptake of  $\text{NH}_3$  on wet surfaces forms a strong sink, which leads to a net negative  $\text{NH}_3$  flux towards the surface (Figure 7d). Fluxes of both  $\text{NO}_x$  and  $\text{NH}_3$  show a strong divergence, countering the concept of a constant deposition velocity.

The temporal development of the domain averaged concentrations (Figure 7e) shows similar trends for the two species. Values hover around the background values during the day, with a significant increase in the evening. This increase can be

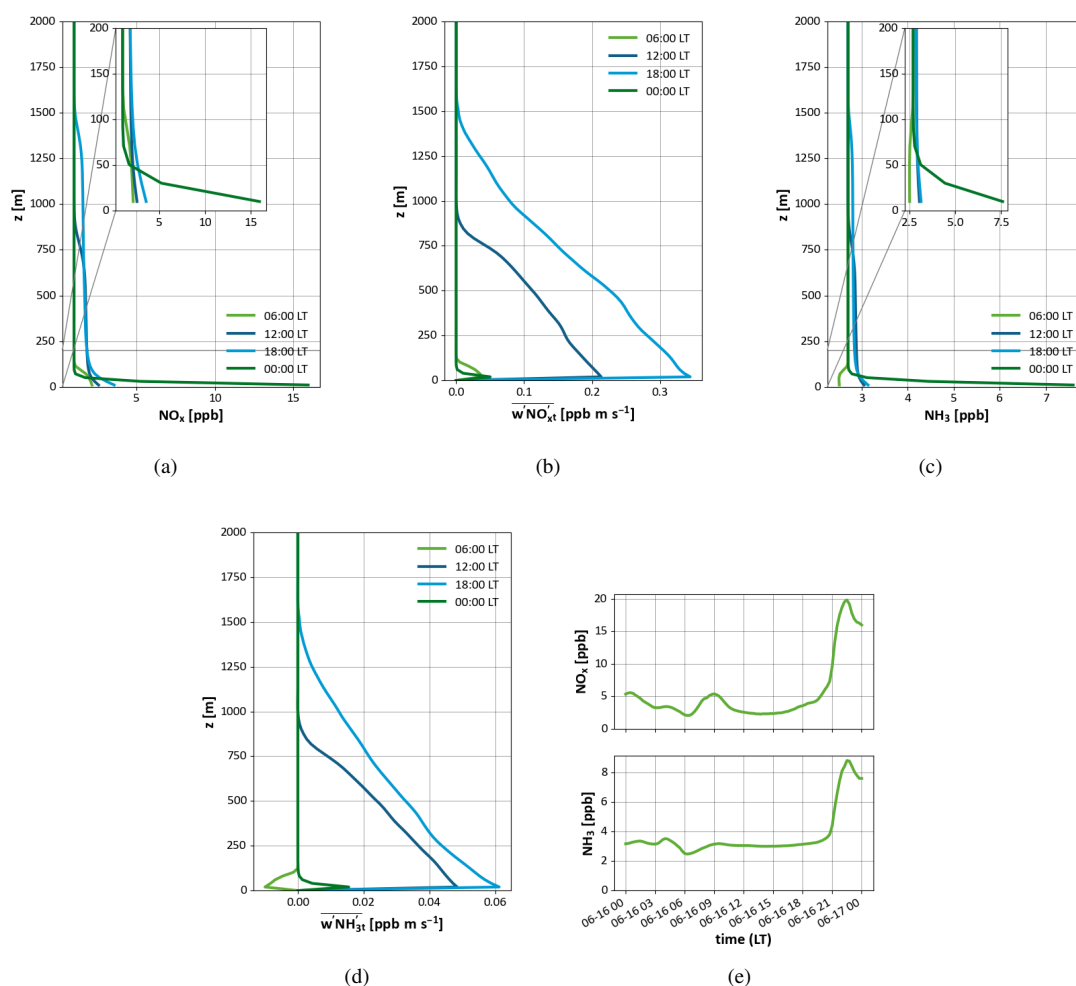


**Figure 7.** Vertical profiles at different times of  $\text{NO}_x$  (a) and  $\text{NH}_3$  concentrations (c), the total turbulent fluxes of both species (b & d), and the temporal development of their domain averaged concentrations (at  $z=10$  m). In (a) and (b) a zoom-in on the lowest 200 m is shown inset.

explained by the fast collapse of the boundary layer (Figure 5d) and by the fact that the emissions from evening traffic are still high, while atmospheric mixing has already subsided.

385 Figure 8a shows the concentration distribution in the domain at 08:00 LT in the lowest layer of the model. The highways clearly show up as the main sources of  $\text{NO}_x$ , producing a local increment of more than  $15 \mu\text{g m}^{-3}$  which is dispersed downwind. In addition, a few other strong sources (mainly industrial) are visible at different locations in the domain. The plumes of  $\text{NO}_x$  generated by highway traffic can still be discerned visibly from the background at 2 - 3 km from the source. The emitted nitrogen oxides are carried downwind, undergoing vertical mixing which causes the near-ground concentrations to reduce away  
 390 from the source. The atmospheric mixing depends on the LU adjacent to the highways, as the concentrations trail off at a lower rate over surfaces with a low roughness (grass) compared to high roughness (forest). The concept of blending distance can be

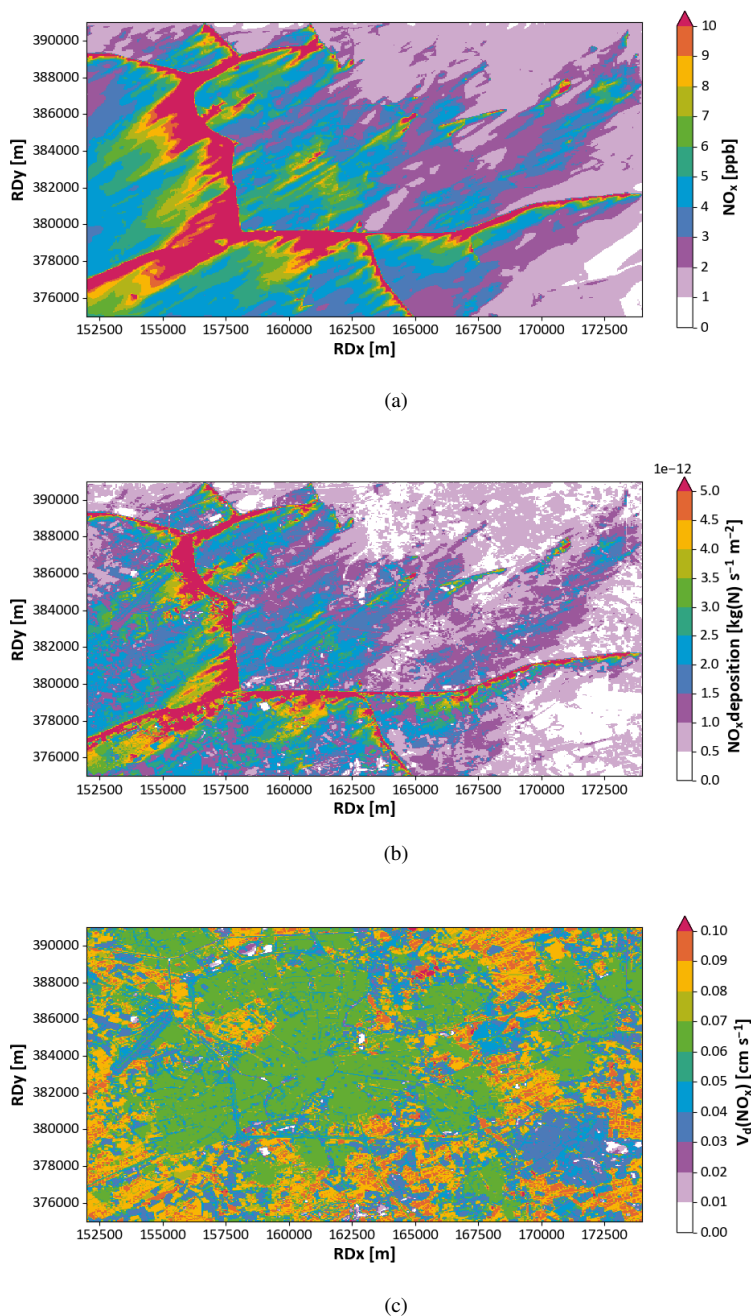


**Figure 8.** Distribution of  $\text{NO}_x$  concentration in the lowest layer of the model ( $z=10$  m) (a), distribution of the deposition flux of  $\text{NO}_x$  (b) and distribution of (c) the deposition velocity of  $\text{NO}_x$  over the domain at 08:00 LT. Note that  $\text{NO}_x$  is deposited as  $\text{NO}_2$ .

used to quantify the distance over which emission plumes travel before they are well mixed with the background concentration distribution (Schulte et al., 2022).



The lowest concentrations are found at the East and North border of the domain, and it is the boundary conditions imposed on the model that explain this. At this moment, DALES does not yet support open boundary conditions. Instead, in the present simulations, we imposed a constant concentration on the boundaries (1 ppb, amounting to approx.  $1.3 \mu\text{g m}^{-3}$ ), which ignores the presence of sources outside the domain, but does provide a realistic background concentration for  $\text{NO}_x$ . DALES is currently being extended by implementing the possibility to nest a calculation in a bigger domain, enabling the use of boundary conditions originating from a parent domain from DALES or a regional-scale atmospheric model (Liqui Lung et al., 2024). This will enable setting realistic boundary conditions with a more accurate background concentration, and incorporating the effect of plumes generated outside the domain.

The concentration difference between the lowest layer of the atmosphere and the compensation point (which is 0 for  $\text{NO}_x$ ) is the driving force of the deposition flux (Figure 8b). The deposition velocity (Figure 8c) is the conversion factor between this concentration difference and the deposition flux. Note that we treated  $\text{NO}_x$  as  $\text{NO}_2$  in our deposition calculations, since in the atmosphere, NO emissions are quickly chemically converted to  $\text{NO}_2$ . Due to its LU dependence, the deposition velocity shows a clear footprint of the LU map. Grassland and open fields show low values ( $0.04 \text{ cm s}^{-1}$ ) for deposition velocity, increasing a little for urban areas ( $0.06 \text{ cm s}^{-1}$ ) and reaching maximum values over forests ( $0.08 \text{ cm s}^{-1}$ ). For  $\text{NO}_x$  these differences are mainly due to the difference in roughness length between the LU types.

The  $\text{NH}_3$  concentration field at 08:00 LT mainly reflects the emissions from agriculture, and hence we find concentration maxima near farm locations at the northern and western edges of the domain (Figure 9a). Also the areas downwind of the highways show elevated concentrations. The atmospheric lifetime of a primary air pollutant and thus its traveling distance is governed by an intricate balance between height of emission, advection and turbulent transport, as well as the removal rates by dry and wet deposition. Specifically for reactive and water soluble pollutants emitted close to ground level, like  $\text{NH}_3$ , the travel distance is shortened by deposition fluxes. This means that species are allowed to travel further over land with a low deposition flux, like grassland and urban areas. Forests are effective to shorten travel distances.

The modeled  $\text{NH}_3$  deposition fluxes are about an order of magnitude larger than those of  $\text{NO}_x$  (Figure 9b). Just as for  $\text{NO}_x$ , the influence of the LU is clearly visible in the  $\text{NH}_3$  deposition flux: smallest fluxes are calculated over urban areas and water bodies, whereas the largest deposition fluxes are found over forest areas. Striking features are modeled near the transition from agricultural land (pastures and cropland) to forest in the northeastern part of the domain (indicated by the box in Fig.9b): here, plumes enriched with  $\text{NH}_3$  are advected from a smooth to a rough surface. Over the rough surface, the turbulent exchange is enhanced, which leads to rapid deposition of  $\text{NH}_3$ . Further into the forest the deposition fluxes become smaller than near the transition. This shows that a high resolution, turbulence resolving model like DALES is uniquely suited to simulate this kind of small-scale features, in which the interactions between the turbulent transport and the change in local LU together determine the deposition flux.

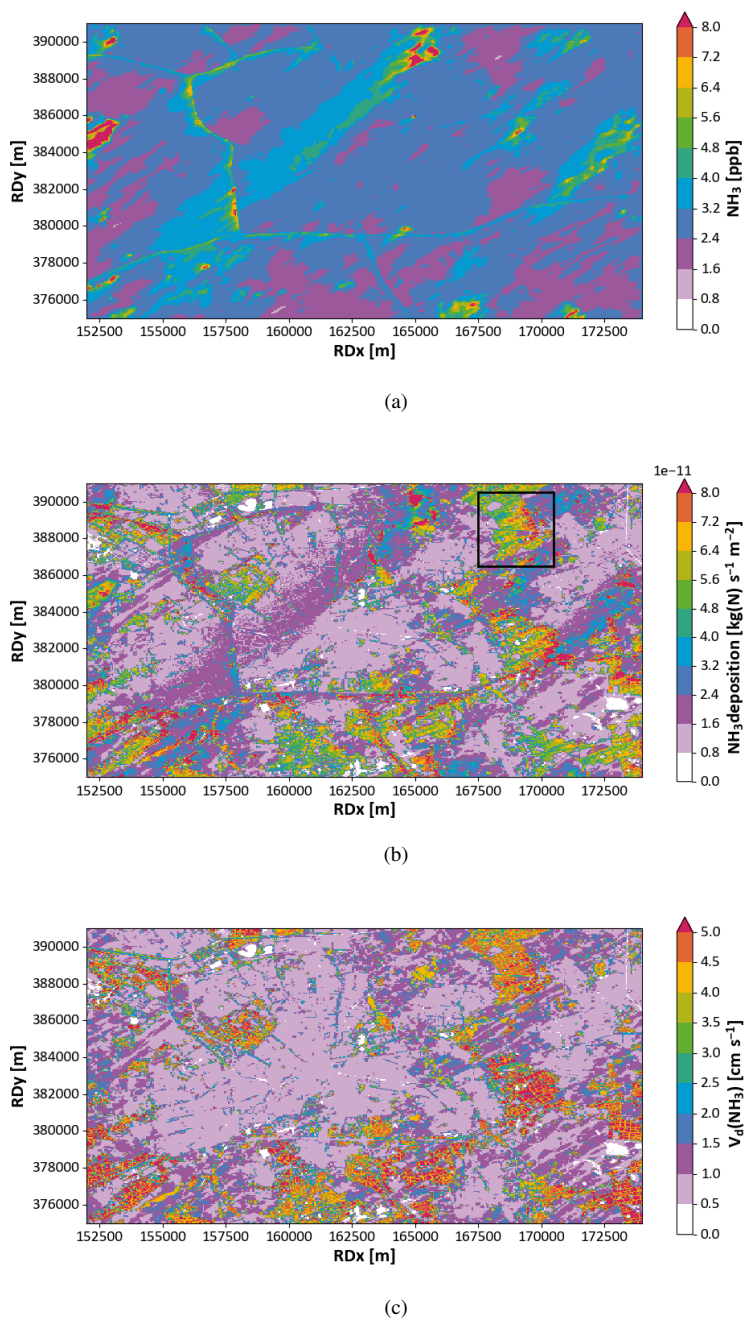


**Figure 9.** Distribution of  $\text{NH}_3$  concentration in the lowest layer of the model ( $z=10$  m) (a), distribution of the deposition flux of  $\text{NH}_3$  (b) and distribution of (c) the deposition velocity of  $\text{NH}_3$  over the domain at 08:00 LT.





## 425 4 Conclusions

Studying the fate of reactive nitrogen compounds in a complex landscape, while accounting for the interplay between dispersion, chemistry and deposition processes, requires a detailed model setup at very high spatial and temporal resolution. We have taken the first steps in preparing the Dutch Atmospheric Large Eddy Simulation (DALES) model for such realistic applications. As a first step we successfully integrated the dry deposition module DEPAC in DALES, supported by a flexible land use  
430 definition. Also, we provided high-resolution emissions of  $\text{NO}_x$  and  $\text{NH}_3$  for the model system.

In a case study for the Eindhoven region we found that DALES is able to reproduce the main features of the boundary layer development and diurnal cycle of local meteorology well, with the exception of the evening transition. DALES calculates the dispersion and deposition of  $\text{NO}_x$  and  $\text{NH}_3$  in great spatial detail, clearly showing the influence of local land use patterns on removal efficiencies and mixing characteristics. This shows the promise of the model for deposition studies in complex  
435 landscapes. To further develop the system for realistic applications we are working on the detailing of the emissions on the required scale, the integration of gas phase chemistry, inorganic aerosol formation and the accommodation of open boundary conditions. In particular regarding emissions, the adoption of a dynamic scheme will reduce the uncertainty of emission fluxes and local concentration estimates.

*Code availability.* DALES is released under the GPLv3 license and it is made available to the general public on the Github repository found  
440 at GitHub - dalesteam/dales: Dutch Atmospheric Large-Eddy Simulation model. The calculations in this paper were performed on the basis of branch '4.4\_Ruisdael\_deposition' ([https://github.com/dalesteam/dales/tree/4.4\\_Ruisdael\\_deposition](https://github.com/dalesteam/dales/tree/4.4_Ruisdael_deposition)). The exact version of the model used to produce the results used in this paper is archived on Zenodo at <https://doi.org/10.5281/zenodo.14843310> (Geers et al., 2025).



## Appendix A: DEPAC parameters

**Table A1.** A selection of model parameters for DEPAC deposition model (Van Zanten et al., 2010) and HTESSEL land surface model (ECMWF, 2021; Balsamo et al., 2009).

LU type parameter	aqu	ara	brn	crp	fbd	fce	grs	sem	urb
$b$ (-)	0.0	14.0	0.0	14.0	14.0	14.0	0.0	14.0	0.0
$h$ (-)	0.0	1.0	0.0	2.5	20.0	20.0	0.0	1.0	0.0
$a_{SAI}$ (-)	0.0	1.0	0.0	1.0	1.0	1.0	1.0	1.0	0.0
$b_{SAI}$ (-)	0.0	1.5	0.0	0.5	1.0	1.0	0.0	0.0	0.0
$R_{s,min}$ (s m <sup>-1</sup> )	1.0·10 <sup>9</sup>	180.0	100.0	225.0	250.0	250.0	100.0	150.0	100.0

**Table A2.** Model parameters for soil resistance  $R_{soil}$  (in s m<sup>-1</sup>) (based on Erisman et al., 1994).

LU type species	aqu	ara	brn	crp	fbd	fce	grs	sem	urb
NH <sub>3</sub>	10	100	100	100	100	100	100	100	100
NO <sub>2</sub>	2000	1000	1000	1000	1000	1000	1000	1000	1000
NO	2000	∞	2000	∞	∞	∞	∞	∞	1000





## Appendix B: Land use translation

**Table B1.** Translation table of TOP10NL land use types (in Dutch) to DEPAC land use types

DEPAC LU type	DEPAC short name	TOP10NL LU types
Aquatic	aqu	Waterloop, Meer/plas, Zee, Water droogvallend, Water droogvallend (LAT), Aanlegstijger
Arable land	ara	Akkerland
Barren land	brn	Zand, Weg onverhard, Braakliggend
Permanent crops	crp	Boomkwekerij, Fruitkwekerij, Boomgaard
Broadleaf deciduous forest	fbd	Loofbos, Griend, Populieren, Dodenakker met bos
Coniferous evergreen forest	fce	Naaldbos, Gemengd bos
Grassland	grs	Grasland
Semi-natural	sem	Heide, Duin, Dodenakker
Urban	urb	Weg verhard, Weg half verhard, Weg onbekend, Spoorbaanlichaam, Basaltblokken/steenglouing, Bebouwd gebied, Overig



## 445 Appendix C: Boundary layer height diagnostics

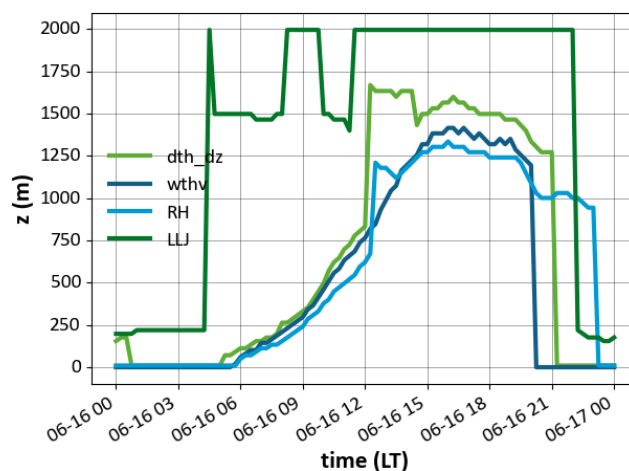


**Figure C1.** Boundary layer height from DALES as diagnosed by 4 different methods: heights of the maximum  $\Delta\theta_v/\Delta h$ , minimum value of  $\overline{w'\theta_v'}$ , maximum value of RH and low level jet, respectively.

*Author contributions.* LG implemented the DEPAC module in DALES and wrote the manuscript. RJ contributed to the model implementation, performed the model calculations, and wrote the manuscript. GT performed model calculations. JV-GdA provided advice on the DALES simulations and the interpretation of the results. MS coordinated the model development and wrote the manuscript. All co-authors commented on the manuscript draft.

450 *Competing interests.* The authors declare no competing interests.

*Acknowledgements.* We acknowledge Bart van Stratum for his work on the land surface module.



## References

- Aan de Brugh, J. M. J., Ouwersloot, H. G., Vilà-Guerau de Arellano, J., and Krol, M. C.: A large-eddy simulation of the phase transition of ammonium nitrate in a convective boundary layer, *Journal of Geophysical Research: Atmospheres*, 118, 826–836, <https://doi.org/10.1002/jgrd.50161>, \_eprint: <https://onlinelibrary.wiley.com/doi/pdf/10.1002/jgrd.50161>, 2013.
- Aleksankina, K., Heal, M. R., Dore, A. J., Van Oijen, M., and Reis, S.: Global sensitivity and uncertainty analysis of an atmospheric chemistry transport model: the FRAME model (version 9.15.0) as a case study, *Geoscientific Model Development*, 11, 1653–1664, <https://doi.org/10.5194/gmd-11-1653-2018>, publisher: Copernicus GmbH, 2018.
- Balsamo, G., Beljaars, A., Scipal, K., Viterbo, P., Hurk, B. v. d., Hirschi, M., and Betts, A. K.: A Revised Hydrology for the ECMWF Model: Verification from Field Site to Terrestrial Water Storage and Impact in the Integrated Forecast System, *Journal of Hydrometeorology*, 10, 623–643, <https://doi.org/10.1175/2008JHM1068.1>, publisher: American Meteorological Society Section: Journal of Hydrometeorology, 2009.
- Barbaro, E., Krol, M., and Vilà-Guerau De Arellano, J.: Numerical simulation of the interaction between ammonium nitrate aerosol and convective boundary-layer dynamics, *Atmospheric Environment*, 105, 202–211, <https://doi.org/10.1016/j.atmosenv.2015.01.048>, 2015.
- Beare, R. J., Macvean, M. K., Holtzlag, A. A. M., Cuxart, J., Esau, I., Golaz, J.-C., Jimenez, M. A., Khairoutdinov, M., Kosovic, B., Lewellen, D., Lund, T. S., Lundquist, J. K., McCabe, A., Moene, A. F., Noh, Y., Raasch, S., and Sullivan, P.: An Intercomparison of Large-Eddy Simulations of the Stable Boundary Layer, *Boundary-Layer Meteorol*, 118, 247–272, <https://doi.org/10.1007/s10546-004-2820-6>, number: 2, 2006.
- Betts, A. K.: Understanding Hydrometeorology Using Global Models, *Bulletin of the American Meteorological Society*, 85, 1673–1688, <https://doi.org/10.1175/BAMS-85-11-1673>, publisher: American Meteorological Society Section: Bulletin of the American Meteorological Society, 2004.
- Blocken, B.: Computational Fluid Dynamics for urban physics: Importance, scales, possibilities, limitations and ten tips and tricks towards accurate and reliable simulations, *Building and Environment*, 91, 219–245, <https://doi.org/10.1016/j.buildenv.2015.02.015>, 2015.
- Bobbink, R., Hicks, K., Galloway, J., Spranger, T., Alkemade, R., Ashmore, M., Bustamante, M., Cinderby, S., Davidson, E., Dentener, F., Emmett, B., Erisman, J.-W., Fenn, M., Gilliam, F., Nordin, A., Pardo, L., and De Vries, W.: Global assessment of nitrogen deposition effects on terrestrial plant diversity: a synthesis, *Ecological Applications*, 20, 30–59, <https://doi.org/10.1890/08-1140.1>, \_eprint: <https://onlinelibrary.wiley.com/doi/pdf/10.1890/08-1140.1>, 2010.
- Businger, J. A., Wyngaard, J. C., Izumi, Y., and Bradley, E. F.: Flux-Profile Relationships in the Atmospheric Surface Layer, *Journal of the Atmospheric Sciences*, [https://journals.ametsoc.org/view/journals/atmsc/28/2/1520-0469\\_1971\\_028\\_0181\\_fprita\\_2\\_0\\_co\\_2.xml](https://journals.ametsoc.org/view/journals/atmsc/28/2/1520-0469_1971_028_0181_fprita_2_0_co_2.xml), section: Journal of the Atmospheric Sciences, 1971.
- CBS: Bevolking; kerncijfers, 1950–2022, <https://www.cbs.nl/nl-nl/cijfers/detail/37296ned>, last Modified: 2023-03-23T02:00:00+01:00, 2023.
- Clifton, O. E. and Patton, E. G.: Does Organization in Turbulence Influence Ozone Removal by Deciduous Forests?, *Journal of Geophysical Research: Biogeosciences*, 126, e2021JG006362, <https://doi.org/10.1029/2021JG006362>, \_eprint: <https://onlinelibrary.wiley.com/doi/pdf/10.1029/2021JG006362>, 2021.
- Clifton, O. E., Patton, E. G., Wang, S., Barth, M., Orlando, J., and Schwantes, R. H.: Large Eddy Simulation for Investigating Coupled Forest Canopy and Turbulence Influences on Atmospheric Chemistry, *Journal of Advances in Modeling Earth Systems*, 14, e2022MS003078, <https://doi.org/10.1029/2022MS003078>, \_eprint: <https://onlinelibrary.wiley.com/doi/pdf/10.1029/2022MS003078>, 2022.



- Cuijpers, J. W. M. and Duynkerke, P. G.: Large Eddy Simulation of Trade Wind Cumulus Clouds, *Journal of the Atmospheric Sciences*, 50, 3894–3908, [https://doi.org/10.1175/1520-0469\(1993\)050<3894:LESOTW>2.0.CO;2](https://doi.org/10.1175/1520-0469(1993)050<3894:LESOTW>2.0.CO;2), publisher: American Meteorological Society Section: *Journal of the Atmospheric Sciences*, 1993.
- Darbieu, C., Lohou, F., Lothon, M., Vilà-Guerau de Arellano, J., Couvreur, F., Durand, P., Pino, D., Patton, E. G., Nilsson, E., Blay-Carreras, E., and Gioli, B.: Turbulence vertical structure of the boundary layer during the afternoon transition, *Atmospheric Chemistry and Physics*, 15, 10071–10086, <https://doi.org/10.5194/acp-15-10071-2015>, publisher: Copernicus GmbH, 2015.
- Deardorff, J. W.: A numerical study of three-dimensional turbulent channel flow at large Reynolds numbers, *Journal of Fluid Mechanics*, 41, 453–480, <https://doi.org/10.1017/S0022112070000691>, publisher: Cambridge University Press, 1970.
- Dise, N. B., Ashmore, M., Belyazid, S., Bleeker, A., Bobbink, R., De Vries, W., Erisman, J. W., Spranger, T., Stevens, C. J., and Van Den Berg, L.: Nitrogen as a threat to European terrestrial biodiversity, in: *The European Nitrogen Assessment*, edited by Sutton, M. A., Howard, C. M., Erisman, J. W., Billen, G., Bleeker, A., Grennfelt, P., Van Grinsven, H., and Grizzetti, B., pp. 463–494, Cambridge University Press, 1 edn., <https://doi.org/10.1017/CBO9780511976988.023>, 2011.
- ECMWF: IFS Documentation CY47R3 - Part IV Physical processes, <https://www.ecmwf.int/en/elibrary/81271-ifs-documentation-cy47r3-part-iv-physical-processes>, 2021.
- Emberson, L., Simpson, D., Tuovinen, J., Ashmore, M., and Cambridge, H.: Towards a model of ozone deposition and stomatal uptake over Europe, *MSC-W*, 2000a.
- Emberson, L. D., Ashmore, M. R., Cambridge, H. M., and Simpson, D.: Modelling stomatal ozone flux across Europe, *Environmental Pollution*, 2000b.
- Emberson, L. D., Ashmore, M., Simpson, D., Tuovinen, J.-P., and Cambridge, H.: Modelling and Mapping Ozone Deposition in Europe, *Water, Air, & Soil Pollution*, 130, 577–582, <https://doi.org/10.1023/A:1013851116524>, 2001.
- EMEP/CEIP: Present state of emission data, Tech. rep., EMEP, <https://www.ceip.at/status-of-reporting-and-review-results/2023-submission>, 2023.
- Erisman, J. W., Van Pul, A., and Wyers, P.: Parametrization of surface resistance for the quantification of atmospheric deposition of acidifying pollutants and ozone, *Atmospheric Environment*, 28, 2595–2607, [https://doi.org/10.1016/1352-2310\(94\)90433-2](https://doi.org/10.1016/1352-2310(94)90433-2), 1994.
- ESA: Report for Assessment: Earth Explorer 11 Candidate Mission Nitrosat Report for Assessment, Tech. Rep. ESA-EOPSM-NITR-RP-4373, European Space Agency, Noordwijk, The Netherlands, [https://esamultimedia.esa.int/docs/EarthObservation/EE11\\_Nitrosat\\_Report\\_for\\_Assessment\\_v1.0\\_15Sept23.pdf](https://esamultimedia.esa.int/docs/EarthObservation/EE11_Nitrosat_Report_for_Assessment_v1.0_15Sept23.pdf), 2023.
- Ge, X., Schaap, M., and de Vries, W.: Improving spatial and temporal variation of ammonia emissions for the Netherlands using livestock housing information and a Sentinel-2-derived crop map, *Atmospheric Environment: X*, 17, <https://doi.org/10.1016/j.aeaoa.2023.100207>, 2023.
- Geers, L., Janssen, R., Thorkelsdottir, G., Vilà-Guerau de Arellano, J., and schaap, m.: Implementation of a dry deposition module (DEPAC v3.11) in a large eddy simulation code (DALES v4.4), <https://doi.org/10.5281/zenodo.14843310>, 2025.
- Grylls, T., Le Cornec, C. M. A., Salizzoni, P., Soulhac, L., Stettler, M. E. J., and van Reeuwijk, M.: Evaluation of an operational air quality model using large-eddy simulation, *Atmospheric Environment: X*, 3, 100041, <https://doi.org/10.1016/j.aeaoa.2019.100041>, 2019.
- Heinen, M., Mulder, H. M., Bakker, G., Wösten, J. H. M., Brouwer, F., Teuling, K., and Walvoort, D. J. J.: The Dutch soil physical units map: BOFEK, *Geoderma*, 427, 116–123, <https://doi.org/10.1016/j.geoderma.2022.116123>, 2022.
- Hersbach, H., Bell, B., Berrisford, P., Hirahara, S., Horányi, A., Muñoz-Sabater, J., Nicolas, J., Peubey, C., Radu, R., Schepers, D., Simmons, A., Soci, C., Abdalla, S., Abellan, X., Balsamo, G., Bechtold, P., Biavati, G., Bidlot, J., Bonavita, M., De Chiara, G., Dahlgren,



- P., Dee, D., Diamantakis, M., Dragani, R., Flemming, J., Forbes, R., Fuentes, M., Geer, A., Haimberger, L., Healy, S., Hogan, R. J., Hólm, E., Janisková, M., Keeley, S., Laloyaux, P., Lopez, P., Lupu, C., Radnoti, G., de Rosnay, P., Rozum, I., Vamborg, F., Villaume, S., and Thépaut, J.-N.: The ERA5 global reanalysis, *Quarterly Journal of the Royal Meteorological Society*, 146, 1999–2049, <https://doi.org/10.1002/qj.3803>, \_eprint: <https://onlinelibrary.wiley.com/doi/pdf/10.1002/qj.3803>, 2020.
- 530 Heus, T., van Heerwaarden, C. C., Jonker, H. J. J., Pier Siebesma, A., Axelsen, S., van den Dries, K., Geoffroy, O., Moene, A. F., Pino, D., de Roode, S. R., and Vilà-Guerau de Arellano, J.: Formulation of the Dutch Atmospheric Large-Eddy Simulation (DALES) and overview of its applications, *Geoscientific Model Development*, 3, 415–444, <https://doi.org/10.5194/gmd-3-415-2010>, number: 2 Publisher: Copernicus GmbH, 2010.
- 535 Jansson, F., van den Oord, G., Pelupessy, I., Grönqvist, J. H., Siebesma, A. P., and Crommelin, D.: Regional Superparameterization in a Global Circulation Model Using Large Eddy Simulations, *Journal of Advances in Modeling Earth Systems*, 11, 2958–2979, <https://doi.org/10.1029/2018MS001600>, number: 9 \_eprint: <https://onlinelibrary.wiley.com/doi/pdf/10.1029/2018MS001600>, 2019.
- Jonson, J. E., Fagerli, H., Scheuschner, T., and Tsyro, S.: Modelling changes in secondary inorganic aerosol formation and nitrogen deposition in Europe from 2005 to 2030, *Atmospheric Chemistry and Physics*, 22, 1311–1331, <https://doi.org/10.5194/acp-22-1311-2022>, number: 2 Publisher: Copernicus GmbH, 2022.
- 540 Kadaster: Alles over de BAG - Kadaster.nl zakelijk, <https://www.kadaster.nl/zakelijk/registraties/basisregistraties/bag>, 2024.
- Khan, B., Banzhaf, S., Chan, E. C., Forkel, R., Kanani-Sühring, F., Ketelsen, K., Kurppa, M., Maronga, B., Mauder, M., Raasch, S., Russo, E., Schaap, M., and Sühring, M.: Development of an atmospheric chemistry model coupled to the PALM model system 6.0: implementation and first applications, *Geoscientific Model Development*, 14, 1171–1193, <https://doi.org/10.5194/gmd-14-1171-2021>, number: 2 Publisher: Copernicus GmbH, 2021.
- 545 Kim, S.-W., Barth, M. C., and Trainer, M.: Influence of fair-weather cumulus clouds on isoprene chemistry, *Journal of Geophysical Research: Atmospheres*, 117, <https://doi.org/10.1029/2011JD017099>, \_eprint: <https://onlinelibrary.wiley.com/doi/pdf/10.1029/2011JD017099>, 2012.
- KNMI: Clouds - calibrated attenuated backscatter profiles from CHM15k ceilometers in the KNMI observation network, 5 minute averaged data - KNMI Data Platform, <https://datapatform.knmi.nl/dataset/ceilonet-chm15k-backsct-la1-t05-v1-0>, 2024a.
- 550 KNMI: Uurgegevens van het weer in Nederland, <https://www.knmi.nl/nederland-nu/klimatologie/uurgegevens>, 2024b.
- Liqui Lung, F., Jakob, C., Siebesma, A. P., and Jansson, F.: Open boundary conditions for atmospheric large-eddy simulations and their implementation in DALES4.4, *Geoscientific Model Development*, 17, 4053–4076, <https://doi.org/10.5194/gmd-17-4053-2024>, publisher: Copernicus GmbH, 2024.
- 555 Manders, A. M. M., Segers, A. J., and Jonkers, S.: LOTOS-EUROS v2.2.003 Reference Guide, 2022.
- Maronga, B., Banzhaf, S., Burmeister, C., Esch, T., Forkel, R., Fröhlich, D., Fuka, V., Gehrke, K. F., Geletič, J., Giersch, S., Gronemeier, T., Groß, G., Heldens, W., Hellsten, A., Hoffmann, F., Inagaki, A., Kadasch, E., Kanani-Sühring, F., Ketelsen, K., Khan, B. A., Knigge, C., Knoop, H., Krč, P., Kurppa, M., Maamari, H., Matzarakis, A., Mauder, M., Pallasch, M., Pavlik, D., Pfafferoth, J., Resler, J., Rissmann, S., Russo, E., Salim, M., Schrempf, M., Schwenkel, J., Seckmeyer, G., Schubert, S., Sühring, M., von Tils, R., Vollmer, L., Ward, S., Witha, B., Wurps, H., Zeidler, J., and Raasch, S.: Overview of the PALM model system 6.0, *Geoscientific Model Development*, 13, 1335–1372, <https://doi.org/10.5194/gmd-13-1335-2020>, publisher: Copernicus GmbH, 2020.
- 560 NGR: Nationaal georegister, <https://www.nationaalgeoregister.nl/geonetwork/srv/dut/catalog.search#/home>, 2024.



- Nieuwstadt, F. T. M. and Brost, R. A.: The Decay of Convective Turbulence, *Journal of the Atmospheric Sciences*, 43, 532–546, [https://doi.org/10.1175/1520-0469\(1986\)043<0532:TDOCT>2.0.CO;2](https://doi.org/10.1175/1520-0469(1986)043<0532:TDOCT>2.0.CO;2), publisher: American Meteorological Society Section: Journal of the Atmospheric Sciences, 1986.
- NWB: Home :: Nationaal Wegenbestand, <https://www.nationaalwegenbestand.nl/>, 2024.
- Ouwensloot, H. G., Vilà-Guerau de Arellano, J., van Heerwaarden, C. C., Ganzeveld, L. N., Krol, M. C., and Lelieveld, J.: On the segregation of chemical species in a clear boundary layer over heterogeneous land surfaces, *Atmospheric Chemistry and Physics*, 11, 10 681–10 704, <https://doi.org/10.5194/acp-11-10681-2011>, number: 20 Publisher: Copernicus GmbH, 2011.
- PDOK: Introductie - PDOK, <https://www.pdok.nl/introductie/-/article/basisregistratie-topografie-brt-topnl>, 2023.
- Prorail: Spoorkaart, <https://www.prorail.nl/reizen/spoorkaart>, 2020.
- RIVM: Data | Emissieregistratie, <https://www.emissieregistratie.nl/data>, 2018.
- Sauter, F. J., Sterk, H., van der Swaluw, E., Wichink Kruit, R. J., de Vries, W., and Van Pul, W. A. J.: The OPS-model; Description of OPS 5.0.0.0, [https://www.rivm.nl/sites/default/files/2020-10/ops\\_v5\\_0\\_0\\_0.pdf](https://www.rivm.nl/sites/default/files/2020-10/ops_v5_0_0_0.pdf), 2020.
- Schalkwijk, J., Jonker, H. J. J., Siebesma, A. P., and Bosveld, F. C.: A Year-Long Large-Eddy Simulation of the Weather over Cabauw: An Overview, *Monthly Weather Review*, 143, 828–844, <https://doi.org/10.1175/MWR-D-14-00293.1>, publisher: American Meteorological Society Section: Monthly Weather Review, 2015.
- Schulte, R. B., van Zanten, M. C., van Stratum, B. J. H., and Vilà-Guerau de Arellano, J.: Assessing the representativity of NH<sub>3</sub> measurements influenced by boundary-layer dynamics and the turbulent dispersion of a nearby emission source, *Atmospheric Chemistry and Physics*, 22, 8241–8257, <https://doi.org/10.5194/acp-22-8241-2022>, number: 12 Publisher: Copernicus GmbH, 2022.
- Simpson, D., Benedictow, A., Berge, H., Bergström, R., Emberson, L. D., Fagerli, H., Flechard, C. R., Hayman, G. D., Gauss, M., Jonson, J. E., Jenkin, M. E., Nyíri, A., Richter, C., Semeena, V. S., Tsyro, S., Tuovinen, J.-P., Valdebenito, A., and Wind, P.: The EMEP MSC-W chemical transport model – technical description, *Atmospheric Chemistry and Physics*, 12, 7825–7865, <https://doi.org/10.5194/acp-12-7825-2012>, number: 16 Publisher: Copernicus GmbH, 2012.
- Singles, R., Sutton, M. A., and Weston, K. J.: A multi-layer model to describe the atmospheric transport and deposition of ammonia in Great Britain, *Atmospheric Environment*, 32, 393–399, [https://doi.org/10.1016/S1352-2310\(97\)83467-X](https://doi.org/10.1016/S1352-2310(97)83467-X), 1998.
- Suter, I., Grylls, T., Sützl, B. S., Owens, S. O., Wilson, C. E., and van Reeuwijk, M.: uDALES 1.0: a large-eddy simulation model for urban environments, *Geoscientific Model Development*, 15, 5309–5335, <https://doi.org/10.5194/gmd-15-5309-2022>, number: 13 Publisher: Copernicus GmbH, 2022.
- Sutton, M. and Fowler, D.: A model for inferring bi-directional fluxes of ammonia over plant canopies, in: *Proceedings of the WMO conference on the measurement and modelling of atmospheric composition changes including pollutant transport*, pp. 179–182, WMO Geneva, 1993.
- Tomas, J. M., Pourquie, M. J. B. M., and Jonker, H. J. J.: The influence of an obstacle on flow and pollutant dispersion in neutral and stable boundary layers, *Atmospheric Environment*, 113, 236–246, <https://doi.org/10.1016/j.atmosenv.2015.05.016>, 2015.
- Twigg, M. M., Berkhout, A. J. C., Cowan, N., Crunaire, S., Dammers, E., Ebert, V., Gaudion, V., Haaima, M., Häni, C., John, L., Jones, M. R., Kamps, B., Kentisbeer, J., Kupper, T., Leeson, S. R., Leuenberger, D., Lüttchwager, N. O. B., Makkonen, U., Martin, N. A., Missler, D., Mounsor, D., Neftel, A., Nelson, C., Nemitz, E., Oudwater, R., Pascale, C., Petit, J.-E., Pogany, A., Redon, N., Sintermann, J., Stephens, A., Sutton, M. A., Tang, Y. S., Zijlmans, R., Braban, C. F., and Niederhauser, B.: Intercomparison of in situ measurements of ambient NH<sub>3</sub>: instrument performance and application under field conditions, *Atmospheric Measurement Techniques*, 15, 6755–6787, <https://doi.org/10.5194/amt-15-6755-2022>, publisher: Copernicus GmbH, 2022.



- Van Genuchten, M. T.: A Closed-form Equation for Predicting the Hydraulic Conductivity of Unsaturated Soils, *Soil Science Society of America Journal*, 44, 892–898, <https://doi.org/10.2136/sssaj1980.03615995004400050002x>, *\_eprint*: <https://onlinelibrary.wiley.com/doi/pdf/10.2136/sssaj1980.03615995004400050002x>, 1980.
- 605 Van Heerwaarden, C. C., Arellano, J. V.-G. d., Gounou, A., Guichard, F., and Couvreur, F.: Understanding the Daily Cycle of Evapotranspiration: A Method to Quantify the Influence of Forcings and Feedbacks, *Journal of Hydrometeorology*, 11, 1405–1422, <https://doi.org/10.1175/2010JHM1272.1>, number: 6 Publisher: American Meteorological Society Section: *Journal of Hydrometeorology*, 2010.
- Van Pul, W. A. J., Van den Broek, M., Volten, H., Van der Meulen, A., Berkhout, B., Van der Hoek, K., Wichink Kruit, R. J., Huijsmans, J., Van Jaarsveld, J., De Haan, B., and Koelemeijer, R. B. A.: Het ammoniakgat: onderzoek en duiding, Report, Rijksinstituut voor Volksgezondheid en Milieu RIVM, <https://rivm.openrepository.com/handle/10029/257709>, accepted: 2017-02-20T06:56:10 Journal Abbreviation: *The ammonia gap: research and interpretation*, 2008.
- 610 Van Stratum, B. J. H., Siebesma, A. P., Barkmeijer, J., and van Ulf, B.: Downscaling HARMONIE-AROME with Large-Eddy simulation, KNMI Technical report TR378, KNMI, <https://www.knmi.nl/research/publications/downscaling-harmonie-arome-with-large-eddy-simulation-ea1186c2-01eb-4d2c-83de-f0d3be023043>, issue: TR378, 2019.
- 615 Van Stratum, B. J. H., Van Heerwaarden, C. C., and Vilà-Guerau de Arellano, J.: The Benefits and Challenges of Downscaling a Global Reanalysis With Doubly-Periodic Large-Eddy Simulations, *Journal of Advances in Modeling Earth Systems*, 15, e2023MS003750, <https://doi.org/10.1029/2023MS003750>, *\_eprint*: <https://onlinelibrary.wiley.com/doi/pdf/10.1029/2023MS003750>, 2023.
- Van Zanten, M., Wichink Kruit, R., van Jaarsveld, H. A., and van Pul, W. A. J.: Description of the DEPAC module : Dry deposition modelling with DEPAC\_GCN2010, Report, Rijksinstituut voor Volksgezondheid en Milieu RIVM, <https://rivm.openrepository.com/handle/10029/256555>, accepted: 2017-02-20T07:18:38 Journal Abbreviation: *Beschrijving van de DEPAC module : Droge depositie modellering met DEPAC\_GCN2010*, 2010.
- 620 Vilà-Guerau de Arellano, J., Talmon, A. M., and Builtjes, P. J. H.: A chemically reactive plume model for the NO-NO<sub>2</sub>-O<sub>3</sub> system, *Atmospheric Environment. Part A. General Topics*, 24, 2237–2246, [https://doi.org/10.1016/0960-1686\(90\)90255-L](https://doi.org/10.1016/0960-1686(90)90255-L), 1990.
- Vilà-Guerau de Arellano, J., Kim, S.-W., Barth, M. C., and Patton, E. G.: Transport and chemical transformations influenced by shallow cumulus over land, *Atmospheric Chemistry and Physics*, 5, 3219–3231, <https://doi.org/10.5194/acp-5-3219-2005>, publisher: Copernicus GmbH, 2005.
- 625 Vilà-Guerau de Arellano, J., van den Dries, K., and Pino, D.: On inferring isoprene emission surface flux from atmospheric boundary layer concentration measurements, *Atmospheric Chemistry and Physics*, 9, 3629–3640, <https://doi.org/10.5194/acp-9-3629-2009>, publisher: Copernicus GmbH, 2009.
- 630 Vilà-Guerau de Arellano, J., Patton, E. G., Karl, T., Dries, K. v. d., Barth, M. C., and Orlando, J. J.: The role of boundary layer dynamics on the diurnal evolution of isoprene and the hydroxyl radical over tropical forests, *Journal of Geophysical Research: Atmospheres*, 116, <https://doi.org/10.1029/2010JD014857>, 2011.
- Vinuesa, J.-F. and Vilà-Guerau de Arellano, J.: Fluxes and (co-)variances of reacting scalars in the convective boundary layer, *Tellus B*, 55, 935–949, <https://doi.org/10.1046/j.1435-6935.2003.00073.x>, *\_eprint*: <https://onlinelibrary.wiley.com/doi/pdf/10.1046/j.1435-6935.2003.00073.x>, 2003.
- 635 Wen, Y., Zhang, S., Wu, Y., and Hao, J.: Vehicular ammonia emissions: an underappreciated emission source in densely populated areas, *Atmospheric Chemistry and Physics*, 23, 3819–3828, <https://doi.org/10.5194/acp-23-3819-2023>, publisher: Copernicus GmbH, 2023.





- Wesely, M. L.: Parameterization of surface resistances to gaseous dry deposition in regional-scale numerical models, *Atmospheric Environment* (1967), 23, 1293–1304, [https://doi.org/10.1016/0004-6981\(89\)90153-4](https://doi.org/10.1016/0004-6981(89)90153-4), 1989.
- 640 Wesely, M. L. and Hicks, B. B.: Some Factors that Affect the Deposition Rates of Sulfur Dioxide and Similar Gases on Vegetation, *Journal of the Air Pollution Control Association*, <https://www.tandfonline.com/doi/abs/10.1080/00022470.1977.10470534>, publisher: Taylor & Francis Group, 1977.
- Wichink Kruit, R. J. R., van Pul, W. A. J., Otjes, R. P., Hofschreuder, P., Jacobs, A. F. G., and Holtslag, A. A. M.: Ammonia fluxes and derived canopy compensation points over non-fertilized agricultural grassland in The Netherlands using the new gradient ammonia—high  
 645 accuracy—monitor (GRAHAM), *Atmospheric Environment*, 41, 1275–1287, <https://doi.org/10.1016/j.atmosenv.2006.09.039>, 2007.
- Wichink Kruit, R. J. W., van Pul, W. A. J., Sauter, F. J., van den Broek, M., Nemitz, E., Sutton, M. A., Krol, M., and Holtslag, A. A. M.: Modeling the surface–atmosphere exchange of ammonia, *Atmospheric Environment*, 44, 945–957, <https://doi.org/10.1016/j.atmosenv.2009.11.049>, 2010.
- Zhang, Y., ten Brink, H., Slanina, S., and Wyers, P.: The influence of ammonium nitrate equilibrium on the measurement of exchange fluxes  
 650 of ammonia and nitric acid, in: *Studies in Environmental Science*, edited by Heij, G. J. and Erisman, J. W., vol. 64 of *Acid Rain Research: Do we have enough answers?*, pp. 103–112, Elsevier, [https://doi.org/10.1016/S0166-1116\(06\)80277-3](https://doi.org/10.1016/S0166-1116(06)80277-3), 1995.
- Zhong, J., Cai, X.-M., and Bloss, W. J.: Large eddy simulation of reactive pollutants in a deep urban street canyon: Coupling dynamics with O<sub>3</sub>-NO<sub>x</sub>-VOC chemistry, *Environmental Pollution*, 224, 171–184, <https://doi.org/10.1016/j.envpol.2017.01.076>, 2017.